

yields represent overall conversion yields. The tetradecamer contains 11 deoxyadenosine units. Deoxyadenosine is the nucleoside most susceptible to glycoside bond hydrolysis during acid cleavage of the DMT group during each cycle. Figure 8 shows the sizing gel results of all three molecules purified by HPLC as previously described.

Conclusion

The synthesis of oligonucleotides up to 14 units in length is now a routine procedure. The DNA/RNA Synthesizer and reagent kits for the preparation of units up to 14 in length are commercially available. The synthesis can be carried out in any laboratory with the use of the synthesizer and the reagent kits, and no

previous experience in nucleotide synthesis is necessary. The reagent kit is attached to the synthesizer; the sequence is typed into the memory; the start signal is given; and the synthesis continues uninterrupted until it is complete.

This basic procedure also applies to the synthesis of RNA sequences (20).

References and Notes

1. For a general review of these and related areas see the recombinant DNA issue of *Science*, 19 September 1980.
2. A. M. Michelson and A. R. Todd, *J. Chem. Soc.* **1955**, 2632 (1955).
3. H. G. Khorana, *Some Recent Developments in the Chemistry of Phosphate Esters of Biological Interest* (Wiley, New York, 1961), pp. 93-140; *Bioorg. Chem.* **1**, 351 (1978).
4. R. L. Letsinger and K. K. Ogilvie, *J. Am. Chem. Soc.* **89**, 4801 (1967); R. L. Letsinger and V. Mahadevan, *ibid.* **88**, 5319 (1966).
5. F. Eckstein and I. Rizk, *Angew. Chem.* **79**, 684 (1967).
6. C. B. Reese and R. Saffhill, *Chem. Commun.* (1968), p. 767.
7. S. A. Narang, R. Brousseau, H. M. Hsiung, J. J. Michniewicz, *Methods Enzymol.* **65**, 610 (1980).
8. R. L. Letsinger, J. L. Finnan, G. A. Heavner, W. B. Lunsford, *J. Am. Chem. Soc.* **97**, 3278 (1975).
9. K. K. Ogilvie, N. Theriault, K. L. Sadana, *ibid.* **99**, 7741 (1977).
10. K. K. Ogilvie and N. Y. Theriault, *Can. J. Chem.* **57**, 3140 (1979); K. K. Ogilvie and M. J. Nemer, *ibid.* **58**, 1389 (1980).
11. E. C. Blossey and D. C. Neckers, Eds., *Solid Phase Synthesis* (Academic Press, New York, 1975).
12. W. Parr and K. Grohmann, *Tetrahedron Lett.* (1971), p. 2633.
13. H. Koster, *ibid.* (1972), p. 1527.
14. P. Tundo, *Chem. Commun.* (1977), p. 641.
15. K. K. Ogilvie and M. J. Nemer, *Tetrahedron Lett.* (1980), p. 4159.
16. M. D. Matteucci and M. H. Caruthers, *ibid.*, p. 719.
17. J. F. Fritz and J. N. King, *Anal. Chem.* **48**, 570 (1976).
18. P. Tundo and P. Venturello, *J. Am. Chem. Soc.* **101**, 6066 (1979).
19. A. H. Maxam and W. Gilbert, *Methods Enzymol.* **65**, 499 (1980).
20. K. K. Ogilvie, in preparation.
21. We thank K. Deugau for the sequence analysis, and R. May and L. Rothwell for technical assistance.

Airborne Microwave Remote-Sensing Measurements of Hurricane Allen

W. Linwood Jones, Peter G. Black
Victor E. Delnore, Calvin T. Swift

Hurricanes have been called the greatest storms on earth (1). Over the years considerable effort has been devoted to studying their dynamics and developing models for forecasting their intensity and path of travel. Much attention has been focused on the hurricane planetary boundary layer because it is there that convective processes which drive the hurricane's circulation transport heat and moisture from the ocean. Furthermore, it is the winds at the surface that cause the damage at landfall, either directly, or indirectly by the storm surge. The dynamics of these surface winds are

of paramount interest to researchers and forecasters.

Present methods for estimating hurricane-force surface winds often have limited accuracy. For example, estimates derived from aircraft reconnaissance are frequently based on Beaufort state of the sea relations, but the validity of using these relations for hurricane-force winds has not been established. The sustained flight-level wind at 3300 meters and minimum surface pressures (2) are also used to infer maximum surface winds. To date, the only reliable method of obtaining the surface wind speed has been low-level penetration of the hurricane by aircraft equipped with inertial navigation systems.

To improve the reliability of surface wind estimates by applying microwave remote-sensing technology, a cooperative program was begun by the National Oceanic and Atmospheric Administration (NOAA) and the National Aeronautics and Space Administration (NASA).

In August 1980 the Langley Research Center's active and passive microwave sensors were flown into Hurricane Allen on a NOAA aircraft. This article presents the surface wind speed, wind direction, and rain rate inferred from the microwave sensors and compares these findings with data obtained by a P-3 aircraft that flew near the top of the hurricane planetary boundary layer. The results demonstrate the potential for safe and reliable hurricane measurements by aircraft flying at medium to high altitudes.

Background

The use of passive and active microwave techniques for remote sensing of ocean surface winds is well documented (3). The brightness temperature of the ocean is strongly correlated with wind speed since wind creates roughness, foam, and breaking waves (whitecaps) (4-6). Radar backscatter from the sea can be used to measure wind speed (through the proportionality of the Bragg off-nadir radar return to the wind-dependent spectrum of water waves a few centimeters long) and wind direction (through the anisotropic scattering characteristic of the sea surface) (7-9).

The first airborne passive and active observations of a hurricane were conducted during Hurricane Ava (10). However, in this case, the L-band radar (1.3 gigahertz) observations were used only to generate wave images. This type of observation was later quantified in 1976 (11), demonstrating that L-band radar

When this article was written, W. Linwood Jones and Calvin T. Swift were aerospace technologists at the NASA Langley Research Center, Hampton, Virginia 23665. Jones is now project manager, Communications Systems, General Electric Valley Forge Space Center, King of Prussia, Pennsylvania 19406; Swift is now professor of electrical and computer engineering, University of Massachusetts, Amherst 01003. Peter G. Black is a meteorologist at the Hurricane Research Laboratory, National Oceanic and Atmospheric Administration, Coral Gables, Florida 33145. Victor E. Delnore is a senior environmental engineer at Kentron International, Hampton, Virginia 23665.

cross sections obtained in Hurricane Gloria exhibited a weak dependence on wind speed.

The concept of combining active and passive microwave observation techniques was first implemented with a 13.9-GHz system (S-193 RADSCAT) on Skylab. During this experiment the first such measurements for a hurricane were obtained (10, 12). A tropical storm (Christine) was also measured. The results clearly demonstrated the ability to sense wind speed in hurricanes with a microwave scatterometer after regions of heavy rain were eliminated with the radiometer. The same concept was utilized in the design of Seasat microwave instrumentation, although with considerably coarser spatial resolution (20 kilometers for Skylab versus 50 kilometers for Seasat).

Hurricane Allen, 5 August 1980

Allen was the most intense hurricane ever penetrated by aircraft in the North Atlantic region. On 5 and 8 August 1980 the Langley Research Center's airborne microwave scatterometer and stepped-frequency microwave radiometer were

flown on a NOAA C-130 aircraft as part of a three-aircraft experiment conducted by the National Hurricane Research Laboratory.

The track of the hurricane and the location of the 5 August flights are shown in Fig. 1. A NOAA P-3 aircraft flew at an altitude of 450 to 1500 m directly beneath the C-130, which was at 3300 m, to measure the winds near the top of the hurricane planetary boundary layer. The severe turbulence encountered by the airplane at low altitudes (accelerations of +3.2g and -2.5g were experienced) illustrate the hazardous nature of obtaining reliable measurements of near-surface winds. The remote-sensing portion of the experiment is illustrated schematically in Fig. 2.

A composite map of estimated rainfall rate for the first pass of the P-3 aircraft through the eye of Allen is presented in Fig. 3. This map is the result of analysis of the data from the weather radar system on the lower fuselage. (The labeled features in Fig. 3 are keyed to elements in Figs. 4 to 8.) The backscattered power was integrated in range and time (azimuth) so that the measurement uncertainty was reduced to about ± 1 decibel. This integration scheme resulted in a

spatial resolution of about 1 km. However, uncertainties concerning radar calibration, lack of beam filling, and attenuation led to errors of about ± 2 dB in reflectivity or an error factor of about 2 in rain rate. To minimize these uncertainties, radar returns close to the aircraft were used in making the composite, so that no heavy precipitation intervened between the aircraft and the target.

An unusual feature of Allen noted during the experiment was the double eye structure. The outer eyewall (Fig. 3, A) was located 42 km from the center. The maximum winds, which were in the north quadrant, were 80 m per second at flight level, the highest ever measured by hurricane reconnaissance aircraft. The maximum precipitation in the eyewall was located about 5 km radially outward from the maximum wind in the outer eyewall. Using the relationship for mature hurricanes between radar reflectivity Z and rain rate R ,

$$Z = 300 R^{1.35} \quad (1)$$

we obtain maximum rain rates in the eyewall of about 75 millimeters per hour (13). Two major convective regions in the outer eyewall were indicated by the regions of maximum reflectivity in the

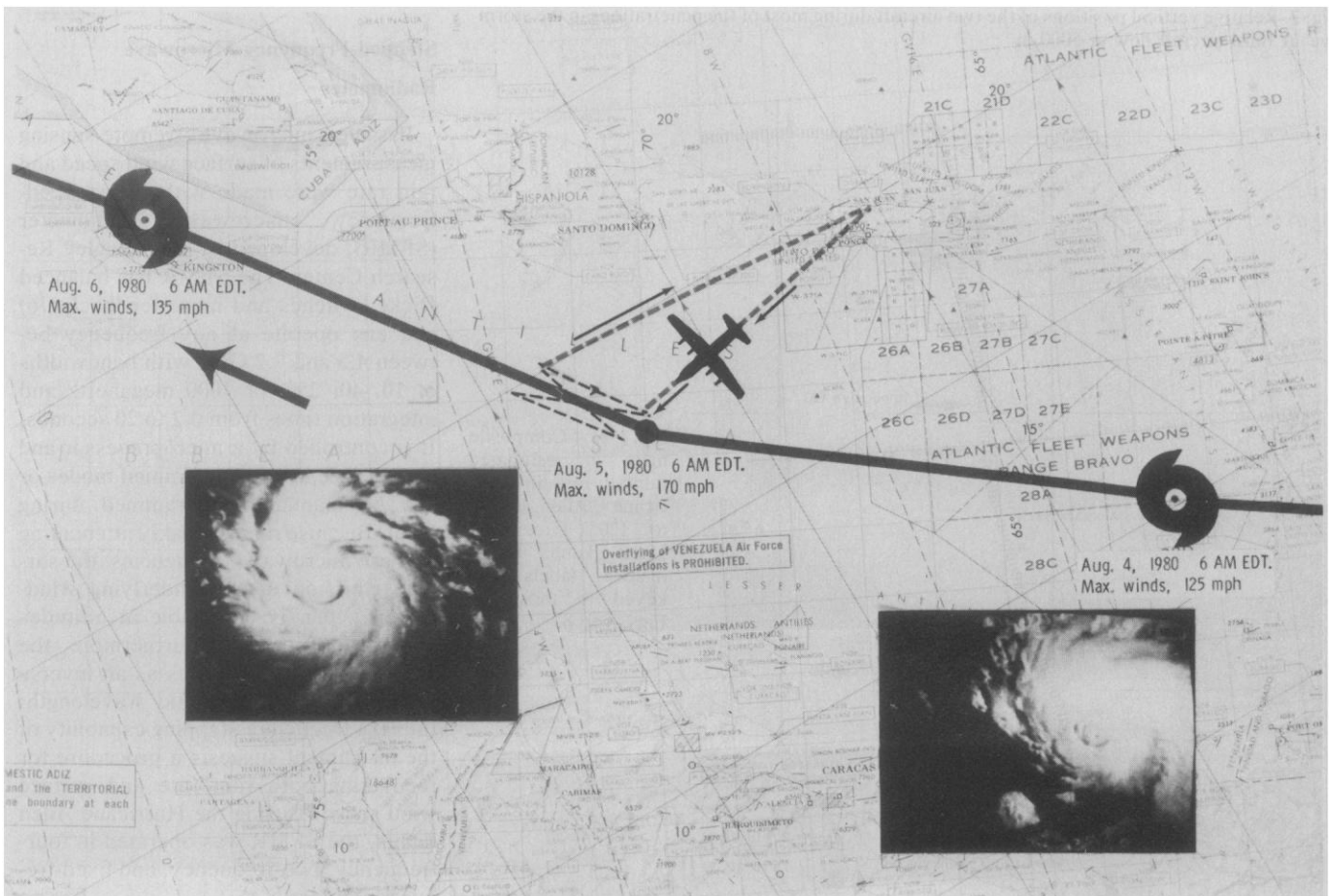


Fig. 1. Storm track of Hurricane Allen, 4 to 6 August 1980, superimposed on an aeronautical navigation chart of the area.

north and south-southeast sectors. These major cores appeared to be stationary, with secondary cores, such as the ones located west and east-northeast of the center, rotating into them. Using information from the C-130 aircraft and the vertically scanning tail radar, we conclude that these convection cores tilted outward and upstream with height at an angle of about 45°. The radius of maximum wind was also greater at higher altitudes.

Precipitation in the inner eyewall (Fig. 3, B) occurred only in the west and north quadrants at about 10 km from the center. The winds averaged 40 to 50 m/sec between the inner and outer eyewalls and then decreased sharply to zero immediately within the inner eyewall. From observations made before and after these penetrations we conclude that the inner eyewall was decaying, with the outer eyewall becoming dominant as its radius slowly decreased with time.

The P-3 aircraft, in its first two penetrations, made wind measurements at an altitude of 1500 m. Comparison with wind profiles obtained later at 450 m suggests that there was little vertical wind shear in this region. Therefore, the assumption is made that the winds at 1500 m are representative of those at the top of the hurricane boundary layer, whose altitude is typically 500 to 600 m (14).

A recent study (15) showed that, for hurricanes moving over tropical waters, the winds at 20 m can be derived from data obtained near the top of the hurricane boundary layer with an accuracy of ± 10 percent. To develop the boundary layer models, buoy measurements were made at nearly the same time as the aircraft measurements. The study also showed that the wind speed at 20 m is approximately 80 percent of that at the flight level. Under conditions of neutral stability, the 80 percent figure had nearly the same accuracy as the boundary layer models. Therefore, for this preliminary study, the winds at 20 m were derived from the aircraft measurements by multiplying them by 0.8. These reduced winds were then compared with the remotely sensed winds.

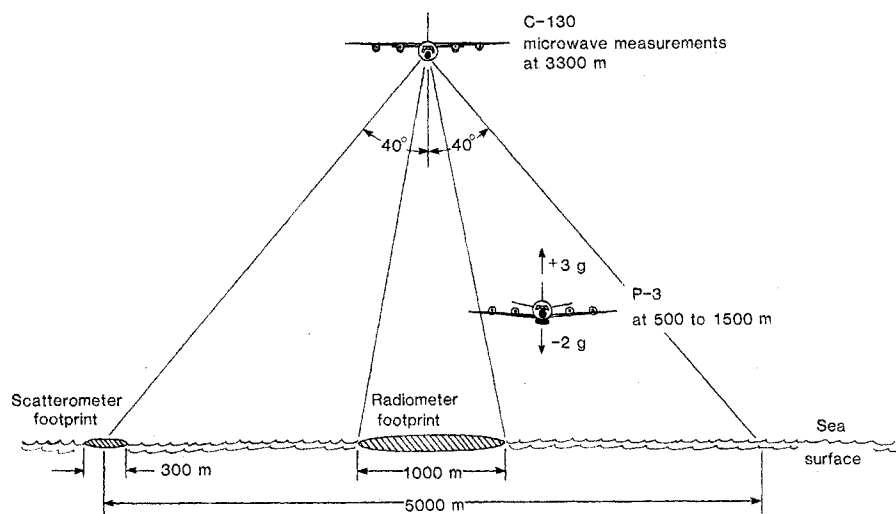


Fig. 2. Relative vertical positions of the two aircraft during most of the penetrations in the storm eye. A third aircraft flew at 5000 m.

Stepped-Frequency Microwave Radiometer

Passive microwave remote-sensing measurements of surface wind speed and rain rate were made with the stepped-frequency microwave radiometer (SFMR), developed by the Langley Research Center. The SFMR has balanced Dicke switches and noise feedback (16) and can operate at any frequency between 4.5 and 7.2 GHz with bandwidths of 10, 40, 250, or 1000 megahertz and integration times from 0.2 to 20 seconds. It is controlled by a microprocessor and can operate in preprogrammed modes or can be manually programmed during flight. Because rain is weakly attenuating at these microwave frequencies, the surface emission of the underlying wind-driven ocean is detectable at altitudes above the rain layer. Furthermore, the attenuation by rain varies as an inverse power of electromagnetic wavelength; thus the frequency-stepping capability of the instrument suggests a procedure for recovering both rain rate and surface wind speed. During the Hurricane Allen flights, the SFMR was operated in four-frequency, two-frequency, and fixed-frequency modes.

A preliminary algorithm was devel-

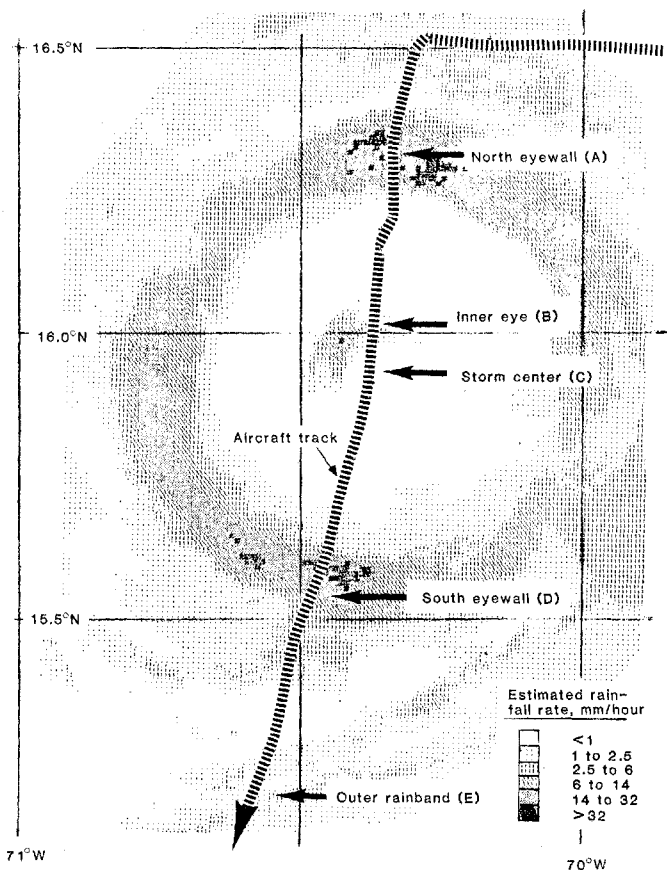


Fig. 3. Composite map of estimated rainfall rate in Hurricane Allen, 1130 to 1205 Greenwich Mean Time. Storm feature labels are keyed to those on Figs. 4 to 8.

oped to compute the surface wind speed and rain rate from the SFMR-measured radiometric brightness temperature at two frequencies. The radiometric brightness temperature, as measured by the SFMR, is the sum of (i) the electromagnetic radiation from the surface, attenuated by the intervening atmosphere, and (ii) the radiation emitted by the intervening atmosphere. Since the sea surface thermodynamic temperature was approximately 28°C, the expected radiometric brightness temperature for a calm sea and clear atmosphere ranges from 113.7 to 116.0 K for 4.5 to 6.6 GHz. The increase in radiometric brightness temperature due to wind speed is approximately $0.7 \text{ K m}^{-1} \text{ sec}^{-1}$ (17) and is almost independent of frequency over the range 4.5 to 7.2 GHz.

The atmosphere between the radiometer and the ocean surface attenuates the electromagnetic surface radiation and also emits electromagnetic radiation. In the microwave frequency region 4.5 to 7.2 GHz the attenuation is a result of the absorption by oxygen molecules, water vapor, nonprecipitating liquid water, and rain.

Within the microwave band of interest, the relative variations in brightness temperature as a function of frequency for the first three sources represent a maximum error of 3 K. This is negligible compared to the rain component; therefore, all dispersive effects are attributed to rain. Assuming that the rain opacity τ_R varies with frequency to the power k , a first-order two-frequency solution to the radiation transfer equation results in the following equation for the attenuation attributable to rain at the lower frequency f_1 :

$$\exp(-\tau_R) = \frac{(\langle T \rangle - TB_2)^{1/2[(f_2/f_1)^k - 1]}}{\langle T \rangle - TB_1} \quad (2)$$

where TB_2 is the measured radiometric brightness temperature at f_2 , TB_1 is the measured radiometric brightness temperature at f_1 , $\langle T \rangle$ is the average temperature of the intervening atmosphere, and τ_R is the opacity at f_1 . In the case of Rayleigh absorption, k would assume a value of 2. Rain attenuation experiments (18) have shown, however, that k can exceed 2. The derivation of Eq. 2 assumes that the surface temperature T_S is equal to $\langle T \rangle$. A second-order expansion indicates maximum residual errors of the order of 1 K.

The other unknown to be solved with the simultaneous equations is the surface emissivity. Here the isothermal condi-

tion of ocean and atmosphere need not be imposed, and the resultant expression for surface emissivity is

$$e = \frac{a \exp(-2\tau_R) - b}{c \exp(-\tau_R) + a \exp(-2\tau_R)} \quad (3)$$

where

$$a = \left[\frac{\langle T \rangle - T_\infty}{\langle T \rangle} \right] e^{-\tau_{O_2}}$$

$$b = \frac{\langle T \rangle - TB_1}{\langle T \rangle}$$

$$c = \frac{T_S - \langle T \rangle}{\langle T \rangle}$$

In the definition for a , $T_\infty = 2.7 \text{ K}$, the Big Bang cosmic residual, and τ_{O_2} is oxygen opacity.

If e_0 is the emissivity of smooth water, then any excess brightness temperature ΔT_w results from wind-driven roughness and foaming. Assuming a linear increase of brightness temperatures with wind speed, extrapolation of the radiative transfer equation in clear air conditions gives

$$\Delta T_w = KW = (e - e_0)(c + a) \quad (4)$$

where $K = 0.7 \text{ K m}^{-1} \text{ sec}^{-1}$ as previously cited, and W is wind speed.

The rain rate R was calculated from the relation

$$R = 320 \tau_{R2} \quad (5)$$

where τ_{R2} is the rain opacity at frequency f_2 . The value 320 corresponds to the constant of proportionality at 6.6 GHz, as given by Gloersen and Barath (19). The choice of 320 also gives results that

are in reasonable agreement with design graphs used for estimating rain degradation of communication links. Efforts will, however, be made to improve the various parameters in the algorithms.

The first pass through Hurricane Allen was from north to south along 70.35°W. During this pass the SFMR was operated in a four-frequency mode, collecting 1-second samples of data sequentially at 4.5, 5.0, 5.6, and 6.6 GHz. The radiometric brightness temperature for these frequencies is shown in Fig. 4. Heavy rain rates in the northern eyewall result in a large separation between the curves for 4.5 and 6.6 GHz around 16.3°N. The presence of the inner eyewall is indicated between 16.1° and 16.0°N, and the center of the eye is at 15.93°N. Some rain is indicated in the southern eyewall at 15.6°N.

The inferred wind speeds for the first pass, as determined with the SFMR, are shown in Fig. 5 with the wind speeds measured by the P-3 aircraft after extrapolation to the 20-m level. Retrievals were performed for values of the rain wavelength scaling factor k from 2 to 4, and $k = 3$ resulted in the best absolute fit to the P-3 wind data. The SFMR measured the surface winds over a dynamic range from nearly 0 m/sec in the eye to approximately 70 m/sec in the eyewall. These measurements show good relative agreement with the in situ measurements over this large dynamic range. However, there is a discrepancy in the measurements of wind gradients in the northern eyewall.

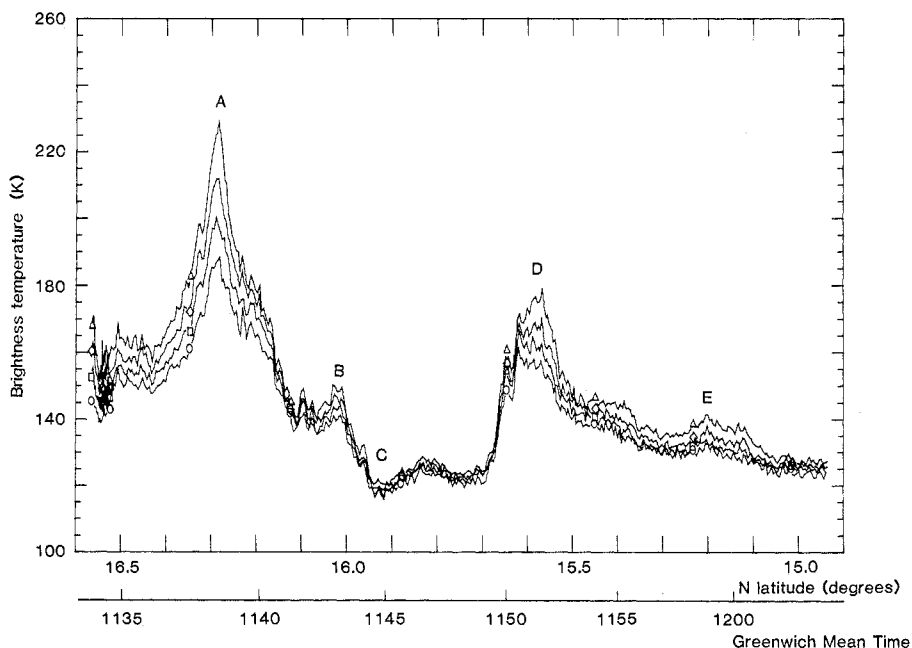


Fig. 4. Radiometer brightness temperature at four frequencies between 4.5 and 6.6 GHz. Higher brightness temperatures are associated with higher frequencies.

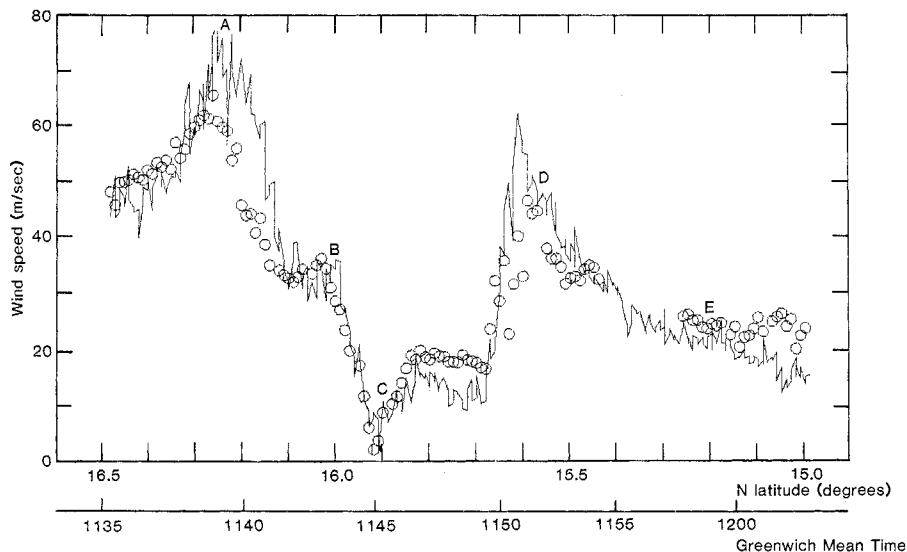


Fig. 5. Surface wind speed derived from magnitude of radiometer brightness temperature (continuous line) and from the P-3 flight-level inertial navigation system (circles).

The rain rates inferred from the SFMR for the first pass are shown in Fig. 6 with the rain rates deduced from the weather radar composite obtained by the P-3. The SFMR algorithm indicated significant rain rates in both the northern and southern portions of the eyewalls; however, the estimate of the rain rate in the southern eyewall is much lower than that determined by the weather radars. This is considered acceptable because the radar-derived rain rate is not known to within a factor of 2. At 16.02°N, in the inner eyewall, both the SFMR and weather radar indicated light rain (2 mm/hour).

Airborne Microwave Scatterometer

Active microwave remote-sensing measurements of surface wind speed and direction were obtained during the Allen flights with the airborne microwave scatterometer (AMSCAT), developed by the Langley Research Center. The physical basis for this technique is Bragg scattering of microwaves from centimeter-length capillary ocean waves. The strength of the radar backscatter (normalized radar cross section, σ°) is a function of the capillary wave amplitude, which in turn is proportional to the wind stress at the sea surface. Furthermore, the radar backscatter is anisotropic; therefore, wind direction can be derived if scatterometer measurements are available from two or more different azimuths.

The AMSCAT is a 14.6-GHz "pencil beam" radar scatterometer that measures the absolute radar cross section of

the ocean. The antenna is a dual-linear polarized parabola (3.5° beam width) mounted on a two-axis, servo-controlled pedestal to provide independent elevation and azimuth antenna pointing. For Allen, this assembly was mounted on the underside of the fuselage beneath the vertical stabilizer (tail section) of the C-130 aircraft. During the experiment σ° was measured at different azimuths with a series of conical antenna scans at 20°, 40°, and 55° angles of incidence. The radar system was under the control of a programmable microprocessor.

The air-sea friction velocity u_* , and the neutral stability wind speed and direction at 19.5 m, \bar{U}_{19} , were inferred by using an algorithm developed for the Seasat-A satellite scatterometer (SASS) (20). The basis of this geophysical algorithm is an empirical "model function" that relates the ocean-normalized radar cross section to friction velocity as a function of incidence angle, azimuth angle, and electric field polarization. The present model function (SASS-I) was developed by using data obtained with an airborne scatterometer and the SASS (21). The σ° data base was correlated with surface wind velocity measured by ships, buoys, or aircraft, with a surface-layer profile model (22) interposed to suppress variability that might be introduced by different measurement heights or atmospheric stratification. The Cardone model (22) specifies the wind profile

$$U = (u_*/k) [\log(z/z_0) - \phi(z/L)] \quad (6)$$

where U is the wind speed, $u_* = (\tau/\rho)^{1/2}$ is the magnitude of the friction velocity (τ is the surface wind stress and

ρ is the density of the air), $k = 0.4$, z is the height, z_0 is the roughness parameter, and L is the stability length from a measurement of wind speed at a given height and the air-sea temperature difference. The dependence of the wind profile on atmospheric stability is incorporated through the function ϕ , which produces a departure from the logarithmic profile.

The neutral stability wind speed was produced at 19.5 m with a logarithmic profile for zero air-sea temperature difference [$\phi(z/L) = 0$]. Thus the neutral stability wind speed is the wind speed that would result from a given friction velocity if the atmosphere were neutrally stratified with an adiabatic lapse rate. Hence the neutral stability wind speed and friction velocity are uniquely related.

If ψ is the angle between the wind direction and the radar look angle, then the azimuthal scattering characteristic is anisotropic due to its dependence on wind direction and is approximated by the Fourier series

$$\sigma^\circ = A_1 \cos \psi + A_2 \cos 2\psi \quad (7)$$

where $A_2 > A_1$. Thus the anisotropy is basically second harmonic, with the strongest return at the upwind and downwind directions and minimum return at the crosswind direction. Further, the data show an upwind-downwind asymmetry, with the upwind peak slightly higher than the downwind peak.

The neutral stability wind speed dependence is included through the coefficients A_1 and A_2 , such that $\sigma^\circ \propto u_*^v$. Here v is the empirical wind speed power law coefficient, which ranges from approximately 1.0 at 20° incidence angle to 2.0 at 55°.

The wind vector algorithm finds the neutral stability wind speed W and wind direction χ which minimize the sum of squares (SOS):

$$\text{SOS} = \sum [\sigma^\circ - F(W, \chi)]^2 / \Delta\sigma^2 \quad (8)$$

where the sum is either a pair of σ° measurements or a group of measurements obtained at different azimuths, $F(W, \chi)$ is the σ° model function (a function of W and χ), and σ° and $\Delta\sigma^\circ$ are the measurement value and its estimated standard deviation, respectively.

During the same north-south pass described in the section on SFMR experimental measurements, AMSCAT was operated in the conical scan mode, sweeping out a 40° cone below the moving C-130. The antenna footprint traced a cycloidal curve on the sea surface. For the programmed rate of the antenna

Fig. 6 (right). Rain rate derived from separation in radiometer brightness temperature at various frequencies (continuous line) and from P-3 weather radar (circles).

scan, approximately 50 seconds were required to gather radar data over a sufficient range of azimuth angles (approximately 140°) to construct a wind vector with the algorithm described above. Figure 2 shows that the AMSCAT footprint was within about 2.5 km of the aircraft track. After the forward motion of the airplane is accounted for, these measurements describe an arc that extends several kilometers along the sea surface for a single wind vector calculation.

A radar signal will scatter and be absorbed as it propagates through air containing water droplets associated with the rain bands of a hurricane. During the first pass through Allen these effects were experienced in the two regions of the eyewall with a high rain rate (Fig. 6). There is no satisfactory means for adjusting the σ^0 algorithm to account for large atmospheric attenuation when the rain rate exceeds 10 to 20 mm/hour. Thus, reasonable wind vectors could not be constructed from the AMSCAT σ^0 data for these two regions of heavy rainfall.

Wind vectors calculated for the first pass through Allen are presented in Fig. 7 (wind speed) and Fig. 8 (wind direction) together with the corresponding inertial navigation system-derived surface values from the P-3 at lower altitudes. The AMSCAT wind speeds and directions are displayed here as short lines rather than as points to represent time- and space-averaging or smearing that was forced by the method of data collection. AMSCAT results are shown only for regions that were relatively free of precipitation.

For these rain-free wind vector calculations the comparison to P-3-derived surface values appears to be good except for the region of wind speed minimum in the eye center (15.93°N). Since the SFMR detected the near zero wind speed (Fig. 5), the C-130 apparently passed through the eye center. Although the AMSCAT, SFMR, and P-3 instruments sampled slightly different radial regions of the vortex wind field, all the data—including data obtained in the small, tight eye—show reasonable agreement.

The remaining AMSCAT-derived wind speeds appear to agree in magnitude and trend with the surface speeds constructed from the P-3 measurements.

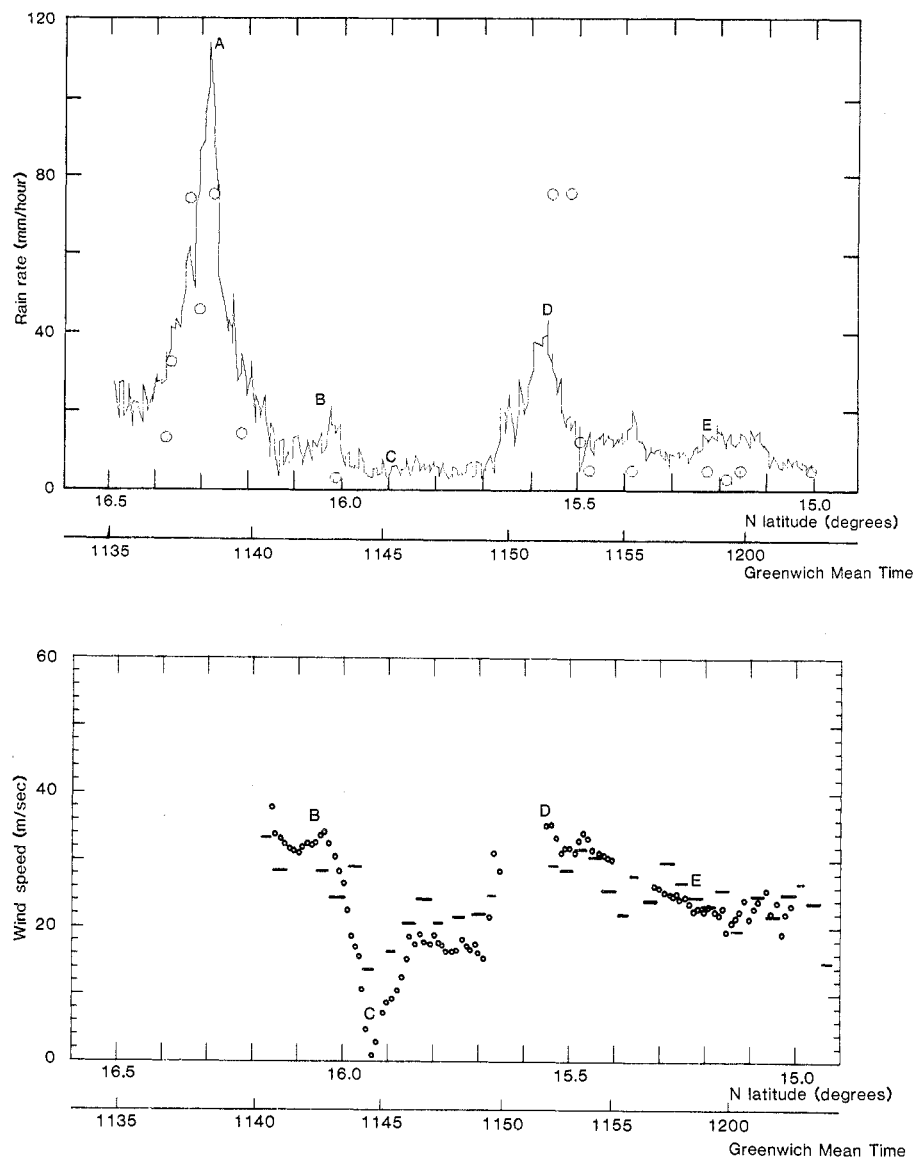


Fig. 7. Surface wind speed derived from scatterometer measurements (bars) and from the P-3 flight-level inertial navigation system (circles). Data are shown only for regions relatively free of precipitation.

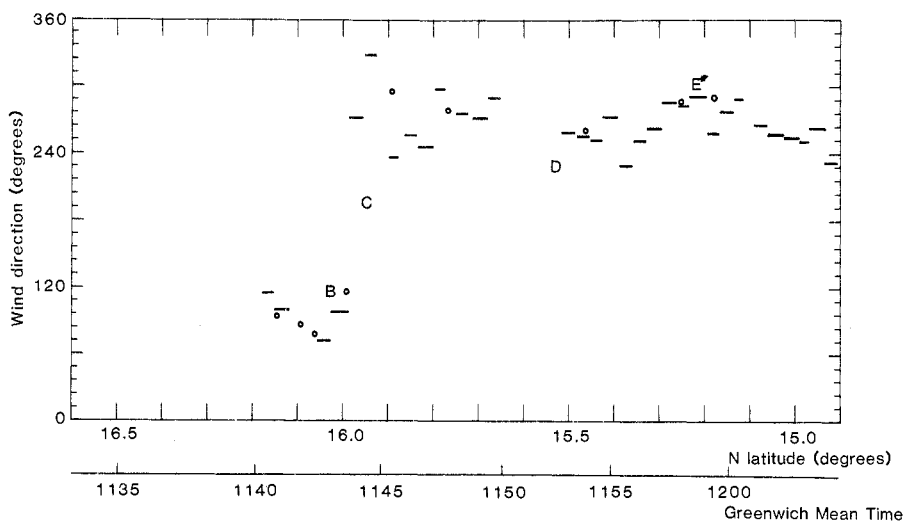


Fig. 8. Surface wind direction derived from scatterometer measurements (bars) and from the P-3 flight-level inertial navigation system (circles). Data are shown only for regions relatively free of precipitation.

Agreement is found over the entire range of wind speeds (14 to 34 m/sec) derived for the rain-free portions of this pass. There is no evidence of any saturation of the radar cross section with increasing wind speed.

Conclusion

The accuracy of the near-surface wind speeds derived from the P-3 measurements is ± 10 percent, with errors due in part to the inertial navigation system measurement itself and to approximations inherent in the hurricane boundary layer model. There may also be small errors in the measurement and processing of the remotely sensed data. Considering these errors and possible misregistration of the two aircraft tracks, certain discrepancies are to be expected. However, when the remotely sensed wind speed, wind direction, and rain rate trends are compared with the values from in situ sources, there is close agreement.

In the future, more sophisticated beam-aiming techniques will be used to form a more optimum sampling scheme. Judicious choice of altitude and incidence angle and adjustment of the antenna azimuth sweep to compensate for the aircraft's speed will allow measurement of σ^0 over the desired range of azimuths

for a reasonably small area of the sea surface. This would be of considerable value in a hurricane, where numerous meteorological phenomena are distributed over relatively short distances. Another improvement would be accurate detection of, and eventual correction for, atmospheric attenuation within the radar beam path.

The data presented here are based on the first of a total of approximately 20 multi-aircraft passes through Hurricane Allen's eye on 5 and 8 August. On many of these passes the AMSCAT antenna was programmed to obtain azimuth sweeps at various incidence angles other than 40° , and also to obtain elevation sweeps at fixed azimuths. The SFMR was operated in a multifrequency mode on all but one pass. In situ measurements are available for nearly all passes.

The data from most of these passes will be analyzed with a view toward optimizing the sensor operating modes and the algorithms for future hurricane experiments. Also, an attempt will be made to process on-board (in real time) at least the SFMR data to surface wind speed and rain rate.

The results of this experiment demonstrate the feasibility of microwave remote sensing techniques to obtain from high altitudes information which is presently obtained at low altitudes and at considerable risk.

Tandem Mass Spectrometry

Fred W. McLafferty

"Needle in a haystack" analytical problems have become important in a variety of areas. Specific compounds which must be recognized in the presence of many others include drugs or disease-indicative compounds in biological fluids, pollutants in environmental samples, chemicals used in the classification of plant and animal species (chemotaxonomy), natural insect attractants (pheromones), flavor- and odor-producing compounds, petroleum and synthetic fuels, process control compounds, chemical warfare agents, and contraband

agricultural products, drugs, and explosives.

Specificity, accuracy, sensitivity, and speed are the key performance characteristics that must justify the cost of the analytical technique chosen. Specificity must be sufficient to distinguish the compound sought (the targeted molecule) from all others present. For quantitation, the specific instrument response must be directly related to the amount of targeted compound present, independent of other components. Sensitivity is a limiting factor for many applications; enzymes,

References and Notes

1. R. C. Gentry, *J. Underwater Sci. Technol.* **2**, 204 (1970).
2. G. D. Atkinson and C. R. Holliday, *Mon. Weather Rev.* **105**, 421 (1977).
3. D. E. Barrick and C. T. Swift, *IEEE J. Oceanic Eng.* **5** (No. 2), 74 (1980).
4. D. B. Ross, J. Conaway, V. J. Cardone, *IEEE Trans. Geosci. Electron.* **8** (No. 4), 326 (1970).
5. W. J. Nordberg, J. Conaway, D. B. Ross, T. Wilheit, *J. Atmos. Sci.* **28**, 429 (1971).
6. D. B. Ross and V. J. Cardone, *J. Geophys. Res.* **79**, 444 (1974).
7. N. W. Guinard, J. T. Ransone, Jr., J. C. Daley, *ibid.* **76**, 1525 (1971).
8. K. Krishen, *ibid.*, p. 6528.
9. W. L. Jones, L. C. Schroeder, J. L. Mitchell, *IEEE J. Oceanic Eng.* **2** (No. 1), 52 (1977).
10. D. B. Ross, B. Chu, W. Brown, J. McFadden, paper presented at the Remote Sensing Symposium, Willow Run Laboratory, Ann Arbor, Mich., 15-20 April 1974.
11. D. E. Weissman, D. King, T. W. Thompson, *J. Appl. Meteorol.* **18**, 1023 (1979).
12. W. J. Cardone et al., *NASA Contract. Rep. CR-147487* (1976).
13. D. P. Jorgenson and P. T. Willis, unpublished manuscript.
14. M. S. Moss and F. J. Merceret, *Mon. Weather Rev.* **104**, 967 (1975).
15. M. D. Powell, *ibid.* **108**, 757 (1980).
16. R. F. Harrington, *NASA Tech. Memo. 81847* (1980).
17. W. J. Webster, T. T. Wilheit, D. B. Ross, P. Gloersen, *J. Geophys. Res.* **81**, 3095 (1976).
18. L. J. Battan, *Radar Observation of the Atmosphere* (Univ. of Chicago Press, Chicago, 1973), p. 73.
19. P. Gloersen and F. T. Barath, *IEEE J. Oceanic Eng.* **2** (No. 2), 172 (1977).
20. W. L. Jones, F. J. Wentz, L. C. Schroeder, *J. Spacecraft Rockets* **15** (No. 6), 368 (1978).
21. L. C. Schroeder, D. H. Boggs, G. Dome, I. M. Halberstam, W. L. Jones, W. J. Pierson, F. J. Wentz, unpublished manuscript.
22. V. J. Cardone, "Specification of the wind distribution in the marine boundary layer for wave forecasting" (Report TR 69-1, School of Engineering and Science, New York University, University Heights, N.Y., 1970).
23. We thank K. Kiley and F. Marks for helping to prepare Figs. 3 and 5. We also acknowledge R. Couch and R. Harrington for instrument support.

drugs, toxins, pheromones, odors, and flavors can be active in picogram concentrations. Speed and applicability are important, for a laboratory's willingness to invest in equipment and trained personnel for a technique will depend on the number and variety of analytical problems it will solve.

Radioimmunoassay (RIA) is a prime example of a technique that combines unusual selectivity and sensitivity (*I*); these properties have led to its widespread use in clinical and research laboratories around the world. For example, 10^{-13} gram of gastrin per milliliter is readily measurable, and steroid molecules differing only in the presence of a hydroxyl group can be distinguished by RIA. Its technical simplicity makes possible a low unit analytical cost and high accuracy with nonprofessional personnel, although several hours are required for an analysis and extensive development of methods may be necessary for a new targeted molecule.

The author is a professor of chemistry at Cornell University, Ithaca, New York 14853.